Supplementary Information

Efficient charge separation at localized 2D ferroelectric domains in perovskite solar cells

Jihoo Lim[1]†, Seungmin Lee[2]†, Hongjae Shim[1]†, Lei Wang[3], Hyeonah Cho[2], Jincheol Kim[4], Claudio Cazorla[5], Yong-Jin Kim[6], Hanul Min[7], Minwoo Lee[1], Xiaojing Hao[1], S. Ravi P. Silva[8], Jan Seidel[3], Dohyung Kim[9,10]*, Jun Hong Noh[2,7]*, Jae Sung Yun[1,8]*

Affiliations:

[1]Australian Centre for Advanced Photovoltaics (ACAP), School of Photovoltaic and Renewable Energy Engineering, University of New South Wales, Sydney, NSW 2052, Australia.

[2]School of Civil, Environmental and Architectural Engineering, Korea University, Seoul 02841, Republic of Korea.

[3]School of Materials Science and Engineering, University of New South Wales, Sydney, NSW 2052, Australia.

[4]Sustainable Energy Research Centre, School of Engineering, Macquarie University, Sydney, NSW 2109, Australia.

[5]Departament de Física, Universitat Politècnica de Catalunya, Campus Nord B4−B5, Barcelona 08034, Spain.

[6]Photovoltaics Research Department, Korea Institute of Energy Research, Daejeon 34129, Republic of Korea.

[7]Department of Integrative Energy Engineering & KU-KIST Graduate School of Converging Science and Technology, Korea University, Seoul 02841, Republic of Korea.

[8]Department of Electrical and Electronic Engineering, Advanced Technology Institute (ATI), University of Surrey, Guildford GU2 7XH, United Kingdom.

[9]Department of Advanced Materials Engineering, Chungbuk National University, Cheongju 28644, Republic of Korea.

[10]Department of Urban, Energy, and Environmental Engineering, Chungbuk National University, Cheongju 28644, Republic of Korea.

*Corresponding author.

Email: dohyungkim@chungbuk.ac.kr, junhnoh@korea.ac.kr, j.yun@surrey.ac.uk

†These authors contributed equally to this work.

Supplementary Text

Possible origin of ferroelectricity in SIG-HPR 2D (MA)PEA_2PbI_4 perovskite

A $(PEA)_2PbI_4$ crystal as a typical 2D Ruddlesden-Popper (RP) perovskite adopts a monoclinic crystal structure with the $P2_1/c$ space group,[1] which can lead to $P2_1$ and Pc polar structures. Tunable ferroelectric properties have been previously observed in MA (methylammonium) RP PEA-incorporated perovskites, attributed to ion translations.[2] Typically, organic cation engineering in molecular ferroelectrics induces lattice distortion and molecular reorientation, leading to order-disorder transitions that alter atomic distributions. Furthermore, ferroelectricity requires the absence of centrosymmetry in the crystal structure, and the strong spin-orbit coupling induced by the heavy Pb atoms can also give rise to the Rashba effect, which has been previously reported in 2D PEA_2PbI_4 perovskites.[3] However, ferroelectricity is not observed in pure PEA_2PbI_4 layered perovskite. As a next step, we investigated PEA_2PbI_4 perovskite in contact with pure $FAPbI_3$ to isolate the effect of the MA cation. However, as shown in **Supplementary Fig. 13**, the results indicate non-ferroelectric behavior, despite exhibiting a higher response than pure 2D PEA_2PbI_4.

A ±90-degree phase change in PFM measurement

In PFM measurements, polarization reversal is typically associated with a 180-degree phase change in the measured signal. This change reflects the transition between two opposite polarization states, such as upward and downward orientations of the ferroelectric domains.
While many data processing schemes represent these two states as being centered at +90° and -90°, the total phase difference between them remains 180°, and such a representation is merely a result of phase offset, or signal centering applied during analysis.
Mathematically, the out-of-plane polarization component can be expressed as:

$$P_z(t) = P_0\sin(\omega t+\phi)$$

where P_0 is the maximum polarization (the amplitude), ω is the angular frequency of the oscillation, and ϕ is the phase. A shift in ϕ by 180° (e.g., from +90° to -90°) leads to a sign inversion of $P_z(t)$, indicating a complete polarization reversal at time.
Therefore, although a 90° phase shift appears in certain contexts due to how the phase reference is defined, it does not correspond to a partial polarization flip. Rather, the ±90° phase states commonly reflect two opposite polarization directions, and a shift between them should be understood as a full polarization reversal.

Experimental Section

Materials:

Lead iodide (PbI_2), and lead bromide ($PbBr_2$) were purchased from Tokyo Chemical Industry (TCI). Phenethylammonium iodide (PEAI), formamidinium iodide (FAI), methylammonium bromide (MABr), and methylammonium chloride (MACl) were purchased from Greatcell Solar Materials. 2,2′,7,7′-tetrakis(N,N-di-4-methoxyphenylamine)-9,9′-spirobifluorene (Spiro-OMeTAD) was purchased from MS solution. Tris(2-(1H-pyrazol-1-yl)-4-tert-butylpyridine)cobalt(III) tri[bis(trifluoromethane)sulfonimide] (cobalt-TFSI) was purchased from Lumtec. Bis(trifluoromethanesulfonyl)imide (Li-TFSI), 4-tertbutylpyridine (TBP), dimethylformamide (DMF), dimethyl sulfoxide (DMSO), urea, hydrochloric acid (HCl), mercaptoacetic acid, potassium chloride (KCl), Chlorobenzene (CB), and acetonitrile (ACN) were purchased from Sigma-Aldrich. 2-methoxyethanol (2-Me) and Tin(II) chloride dihydrate ($SnCl_2{\cdot}2H2O$) were purchased from Alfa Aesar.

Device fabrication:

For $FAPbI_3$ powder synthesis, PbI_2 and FAI were dissolved in 2-Me to prepare a 0.8M precursor solution, then the solution was stirred for 1 hour. The prepared solution was filtered with a 0.2 micrometer PTFE filter, and then heated to 120 °C in an oil bath for 3 hours. Synthesized $FAPbI_3$ powder was filtered using a suction flask and baked at 150 °C for 30 minutes. For $MAPbBr_3$ powder synthesis, $PbBr_2$ and MABr were dissolved in DMF to prepare a 1.67M precursor solution, then the solution was stirred for 1 hour. The prepared solution was filtered with a 0.2 micrometer PTFE filter, and then heated to 70°C in an oil bath for 6 hours. Synthesized $MAPbBr_3$ powder was filtered using a suction flask and baked at 70°C for 1 hour. For preparing the perovskite precursor solution, A 2D precursor solution (0.2M) was prepared by dissolving PEAI and PbI_2 (molar ratio = 2:1) in mixed solvent of DMF and DMSO (v/v = 8:1). The precursor solution was stirred at 60 °C for 1 hour. Before fabricating the 2D perovskite thin film, the solution was filtered using a 0.2 micrometer PTFE filter. For the fabrication of $(FAPbI_3)_{0.95}(MAPbBr_3)_{0.05}$, 3D perovskite precursor solution (1.55M) was prepared by dissolving $FAPbI_3$ and $MAPbBr_3$ in mixed solvent of DMF and DMSO (v/v = 7.5:1). MACl (35 mol% relative to 3D perovskite) was added to the precursor solution. The prepared solution was stirred for 2 hours. Before fabricating the 3D perovskite film, the solution was filtered using a 0.45 micrometer PTFE filter. For the fabrication of $FAPbI_3$, the $FAPbI_3$ precursor solution was prepared in the same manner by replacing the amount corresponding to the moles of $MAPbBr_3$ with $FAPbI_3$. For 2D perovskite thin film fabrication, Tin-doped indium oxide substrate (ITO) was sequentially cleaned with detergent, deionized water, acetone, and isopropyl alcohol using a sonicator for 15 minutes. Then, the cleaned ITO was treated with ultraviolet-ozone for 15 minutes to improve the wetting of the precursor solution. The 2D perovskite solution was coated on the ITO substrate at 5100 r.p.m. for 30 seconds. Then, diethyl ether (1 ml) was quickly poured onto the spinning substrate 10 seconds before the end of the program. Subsequently, the sample was transferred to a hot plate set to 100 °C and heat-treated for 5 minutes. For electron-transporting layer fabrication, Patterned Asahi FTO glass of 1 inch × 1 inch was washed with detergent, deionized water, acetone, and isopropyl alcohol, each for 15 minutes using the sonicator. Then, the cleaned substrate was heat-treated at 450 °C for 1 hour to eliminate residue of organic components. Tin oxide (SnO_2) was deposited as an electron-transporting layer through chemical bath deposition (CBD). The CBD solution was prepared using $SnCl_2{\cdot}2H_2O$, urea, HCl, and mercaptoacetic acid according to a previous report.[4] Prepared FTO glasses were vertically placed inside the CBD solution. The reaction vessel was transferred to an oven set to 90 °C and kept for 6 hours. The substrate with the SnO_2 deposit was withdrawn from the vessel, and then washed with deionized water for 30 minutes. The substrate with FTO/SnO_2 layer was heat-treated at 150°C for 6 hours under ambient conditions. For 3D perovskite thin film fabrication, the prepared

FTO/SnO_2 substrate was cleaned with ultraviolet-ozone for 15 minutes. KCl (40 mM in deionized water) was coated onto the substrate with 5000 r.p.m. (accelerating at 2000 r.p.m. per second) for 30 seconds, and then thermal annealing was performed at 150 °C for 10 minutes. Bathocuproine (0.2 mg/ml) was additionally applied to the KCl-treated SnO_2 substrate to reduce the residual solvent present in the perovskite thin film. The 3D perovskite solution was coated on the substrate by two consecutive spin-coating steps at 1000 r.p.m. for 5 seconds and at 5000 r.p.m. for 15 seconds. Diethyl ether (1 ml) was slowly poured onto the spinning substrate 5 seconds before the end of the program. The yellow film of the intermediate phase was moved to a hot plate set to 120 °C and heat-treated for 1 hour. For 2D/3D junction perovskite fabrication, a high pressure (SIG-HPR) sample was fabricated using a hot-press method. First, the surface of solid-phase $(PEA)_2PbI_4$ film (2D/ITO) was brought into contact with the surface of the 3D perovskite film (FTO/SnO_2/3D). Second, the stacked substrate (FTO/SnO_2/3D:2D/ITO) was pressed at 25 MPa at a temperature of 60 °C for 10 minutes. Finally, the $(PEA)_2PbI_4$ film on ITO was removed from the stacked substrate. Once this three-step process, namely the solid-phase in-plane growth (SIG), is completed, the 2D perovskite layer is grown on the top of the 3D surface, resulting in an FTO/SnO_2/3D/SIG-2D structure. A low pressure (SIG-LPR) sample was fabricated under 0.65 kPa of the pressure, and the other conditions were performed in the same manner as the HP sample. For hole-transporting layer and counter electrode fabrication, the Spiro-OMeTAD solution was prepared by dissolving 100 mg of Spiro-OMeTAD in 1.1 ml of chlorobenzene, with the addition of 23 µl of Li-TFSI (540 mg ml^{-1} in ACN), 10 µl of cobalt-TFSI (375 mg ml^{-1} ACN) and 39 µl of TBP. It was coated on FTO/SnO_2/3D or FTO/SnO_2/3D/2D films at 2000 r.p.m. for 30 seconds. A gold counter electrode was thermally deposited under a pressure of 10^{-6} Torr.

Characterization:

Top-view and cross-sectional scanning electron microscope (SEM) images were obtained using a field-emission SEM (S4800, Hitachi) at Korea University. X-ray diffraction (XRD) patterns were measured using an X-ray diffractometer (SmartLab, Rigaku) with an X-ray tube (copper Kα,45kV, 9kW). All XRD measurements were performed at the same scan rate (1° per minute) and interval (0.02°) at the National Center for Inter-university Research Facilities at Seoul National University. All AFM, PFM and KPFM measurements were carried out using a commercial AFM system (AIST-NT smartSPM1000) under N_2 condition at room temperature. Before the measurement, possible contaminants on the surface of the sample were blown away using nitrogen gun. The platinum AFM tips of (HQ:NSC37/Pt) and (HQ:NSC35/Pt) were used for PFM and KPFM measurements, respectively. Bias voltage was applied to the tip during the PFM and KPFM measurements. For PFM measurements, bias voltages ranging from 0 to +2V were applied to the AFM tip in order to induce polarization. White LED was used to illuminate the perovskite film, positioned at an angle of 45° relative to the sample surface to avoid shading from the probe tip. White LED was also used when measuring SPV and illuminated from the glass side of the sample. The solar cells were measured using a Keithley 2400 source meter unit under the illumination of a ClassAAA solar simulator (94043A, Newport). To check the intensity of the illumination, National Renewable Energy Laboratory (NREL)-calibrated reference solar cell (KG-0) was used before the current density -voltage (*J-V*) measurement. An antireflection film and mask, featuring an aperture area of 0.096 cm^2 were equipped with each solar cell. All J-V curves were measured using a reverse direction (from 1.2 V to -0.2 V) and forward direction (from -0.2 V to 1.2 V), with an internal step of 10 mV and a scan rate of 100 mV s^{-1}. External quantum efficiency (EQE) spectra were obtained from 320 nm to 900 nm at an interval of 10 nm (Qunata-X, Newport). Time-dependent stabilized power outputs were measured with a time interval of 0.2 seconds (IviumStat, Ivium Technologies). The device structure of FTO/SnO_2/3D PVSK/(SIG-HPR 2D PVSK)/Spiro-OMeTAD/Au) was used for ELQE measurements, and were scanned by connecting a calibrated silicon photodiode (Hamamatsu, S1227-1010BQ), which has a larger collection area than the device's active area. The inject current, equivalent to the J_{SC} values of the devices and the detected photocurrent of the photodiode were controlled and measured using two source meter units (Keithley 2450), all of which were operated through the "SweepMe!" program. The long-term operation test was conducted using a Keithley 2450 as the source meter. The maximum power point was updated every hour to track the peak device efficiency using a 0.096 cm^2 of aperture area. During these measurements, the device temperature was maintained at 25 °C, following the standard test conditions for ISOS-L1 protocol.

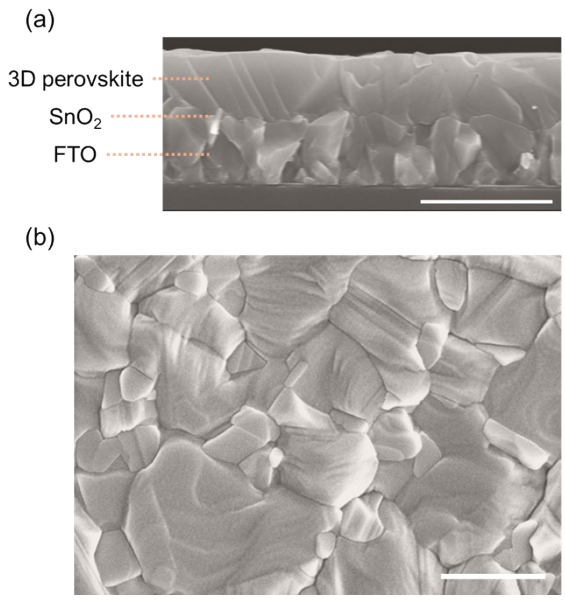

Supplementary Fig. 1. (a) Cross-sectional, and (b) top-view SEM images of SIG-LPR perovskite film. The scale bar represents 1 μm.

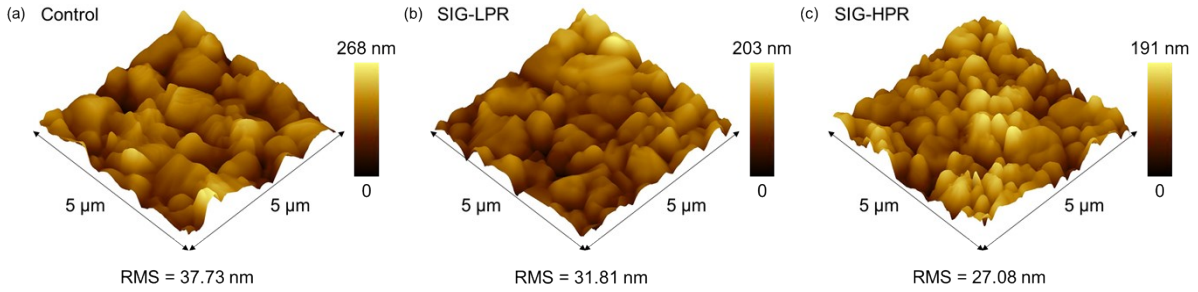

Supplementary Fig.2. 3D AFM topography images and surface roughness of (a) control, (b) SIG-LPR, and (c) SIG-HPR perovskite films.

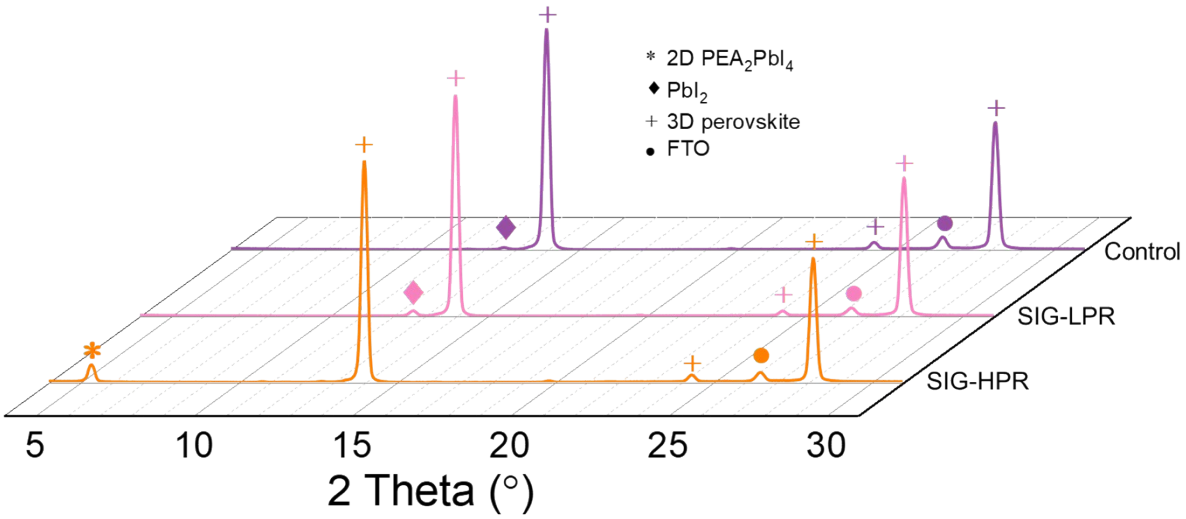

Supplementary Fig.3. XRD patterns of control, SIG-LPR, and SIG-HPR perovskite films.

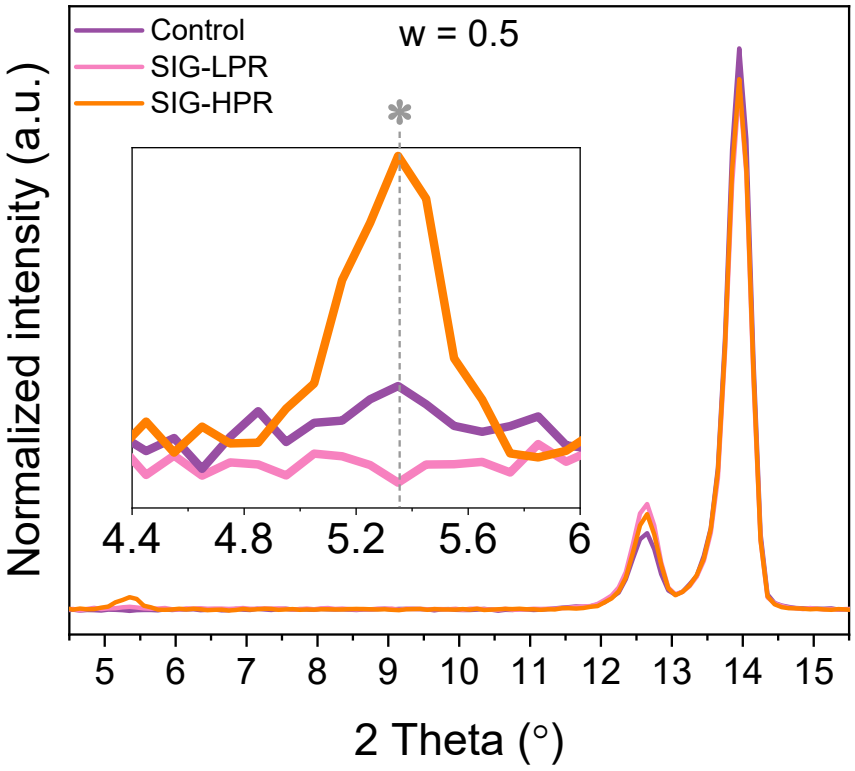

Supplementary Fig.4. Grazing Incidence X-ray Diffraction (GIXRD) measurement of (a) control, SIG-LRP and SIG-HPR perovskite films using an incident angle of 0.5°. The inset shows 2D PEA_2PbI_4 perovskite peak.

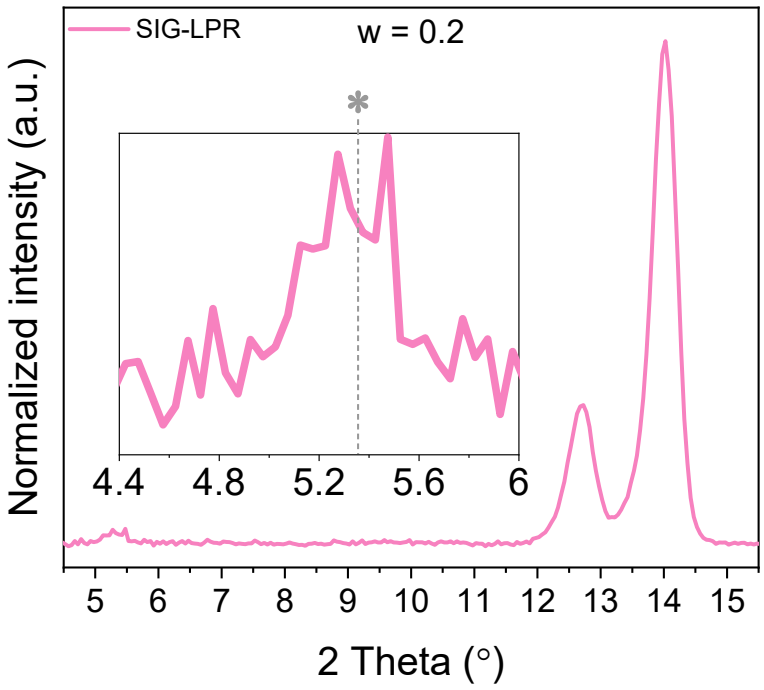

Supplementary Fig.5. GIXRD measurement of SIG-LRP perovskite film using an incident angle of 0.2°. The inset shows 2D PEA_2PbI_4 perovskite peak.

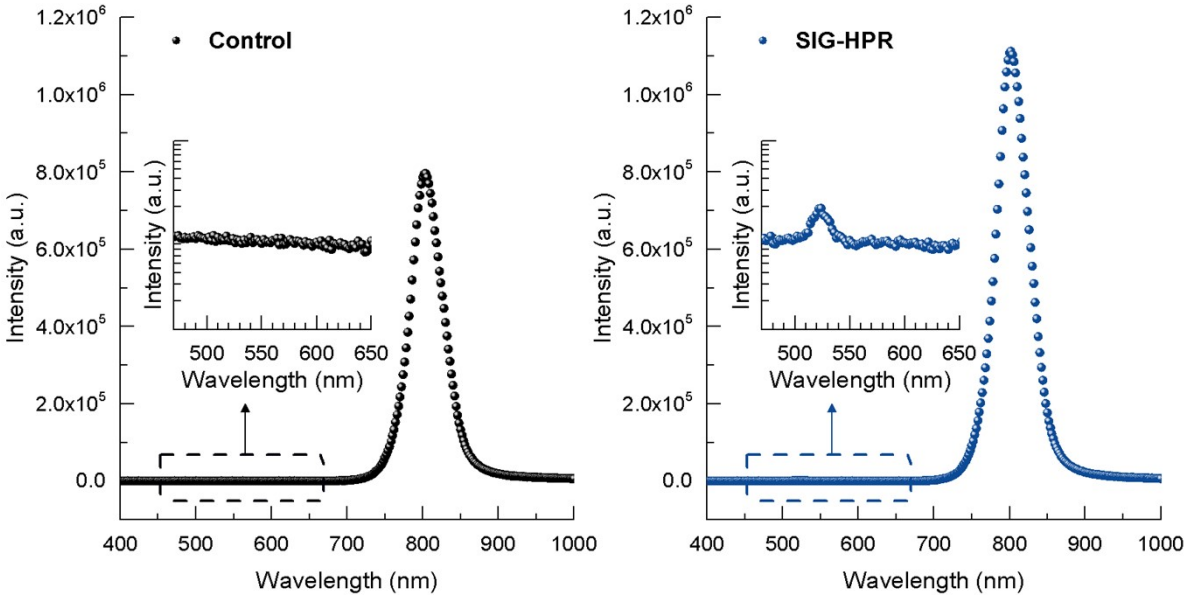

Supplementary Fig.6. PL measurements of control and SIG-HPR perovskite films.

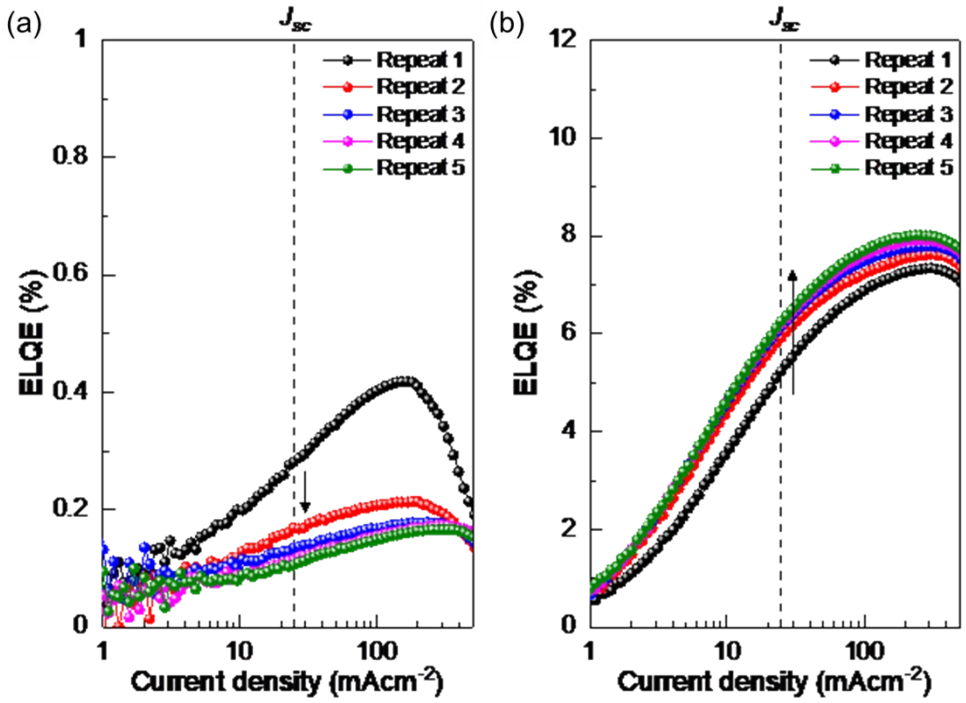

Supplementary Fig. 7. ELQE measurements in accordance with the current density for (a) control, and (b) SIG-HPR device as an LED in dark condition, and the measurements are repeated five times.

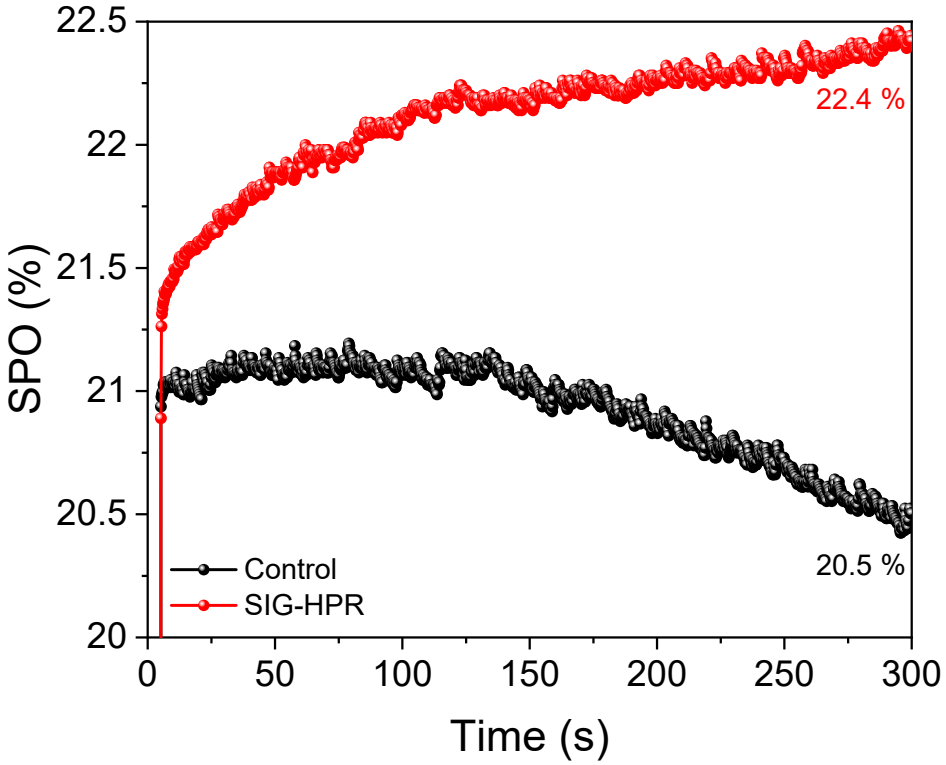

Supplementary Fig. 8. SPO measurements of control, and SIG-HPR devices.

(a)

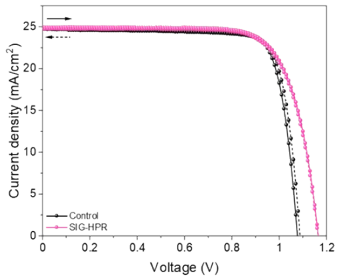

(b)

Control	V_{OC} (V)	J_{SC} (mA/cm²)	FF (%)	PCE (%)
Forward	1.08	24.9	80.5	21.6
Reverse	1.09	24.7	80.4	21.6
Average	1.08	24.8	80.5	21.6
SIG-HPR	**V_{OC} (V)**	**J_{SC} (mA/cm²)**	**FF (%)**	**PCE (%)**
Forward	1.16	24.8	75.8	21.7
Reverse	1.16	24.9	75.9	22.0
Average	1.16	24.9	75.9	21.9

Supplementary Fig. 9. (a) J-V curves, and (b) J-V parameters of control, and SIG-HPR perovskite devices before SPO measurement.

(a)

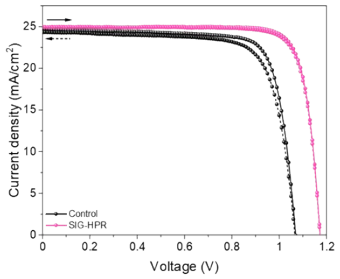

(b)

Control	V_{OC} (V)	J_{SC} (mA/cm²)	FF (%)	PCE (%)
Forward	1.07	24.7	78.2	20.7
Reverse	1.07	24.3	75.3	19.5
Average	1.07	24.5	76.8	20.1
SIG-HPR	**V_{OC} (V)**	**J_{SC} (mA/cm²)**	**FF (%)**	**PCE (%)**
Forward	1.17	25.0	82.8	24.2
Reverse	1.17	25.0	81.8	23.9
Average	1.17	25.0	82.3	24.1

Supplementary Fig. 10. (a) J-V curves, and (b) J-V parameters of control, and SIG-HPR perovskite devices after SPO measurement.

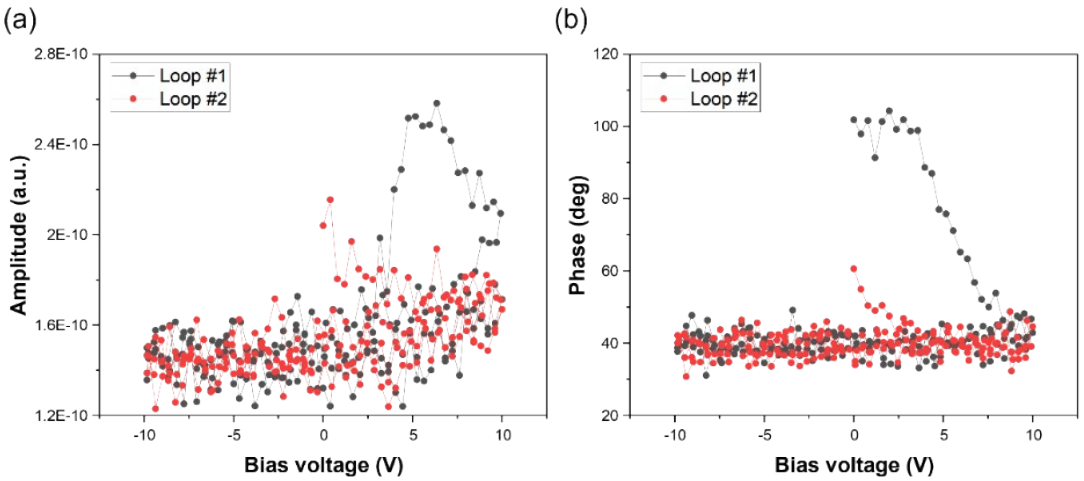

Supplementary Fig. 11. Spectroscopic PFM measurements of pure 2D PEA_2PbI_4 perovskite. (a) PFM amplitude, and (b) PFM phase responses as a function of bias voltages.

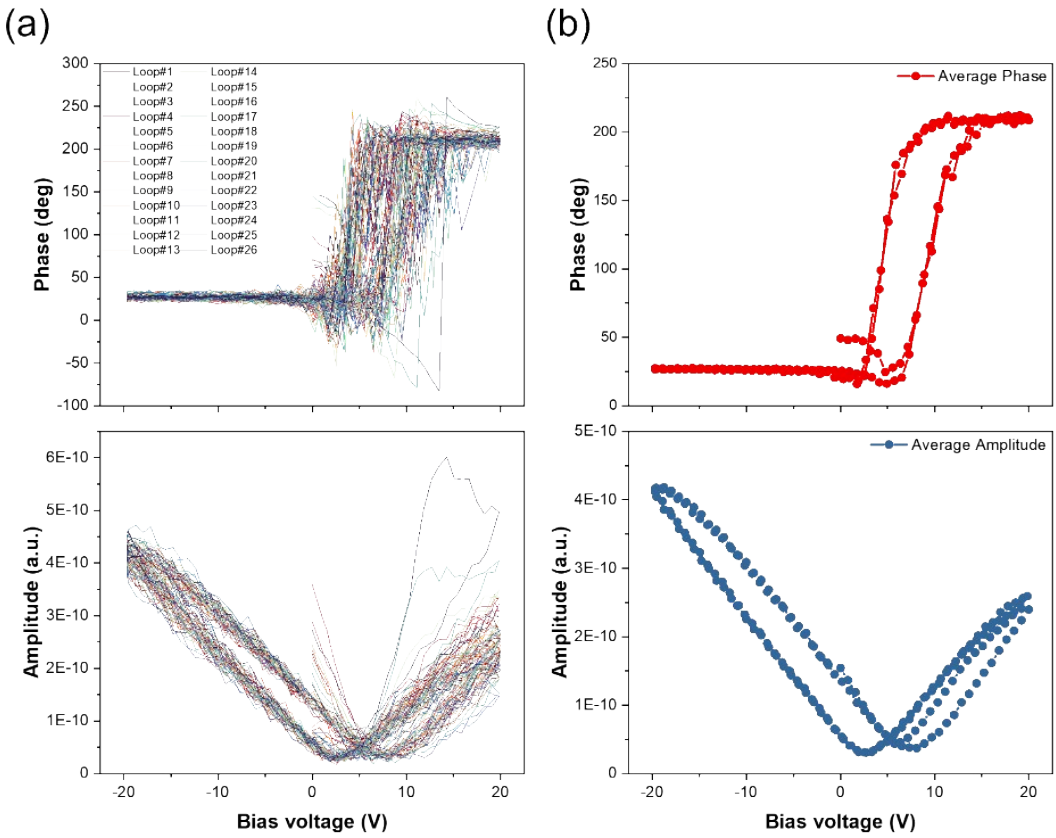

Supplementary Fig. 12. Spectroscopic PFM measurements. (a) Series of PFM loops in phase and amplitude, and (b) averaged signals in 2D PEA_2PbI_4 with $(FAPbI_3)_{0.95}(MAPbBr_3)_{0.05}$ perovskite via SIG process.

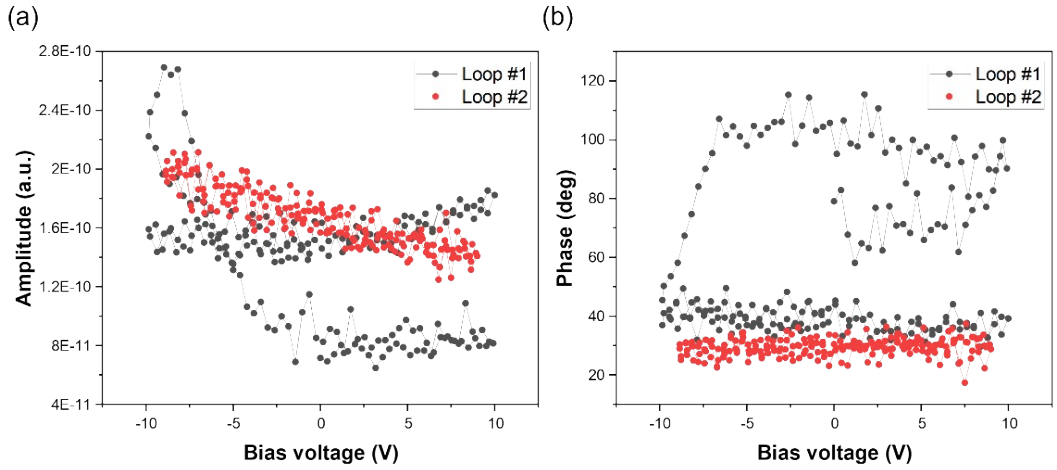

Supplementary Fig. 13. Spectroscopic PFM measurements. (a) PFM amplitude, and (b) PFM phase responses as a function of bias voltages in 2D PEA_2PbI_4 with pure $FAPbI_3$ perovskite via SIG process.

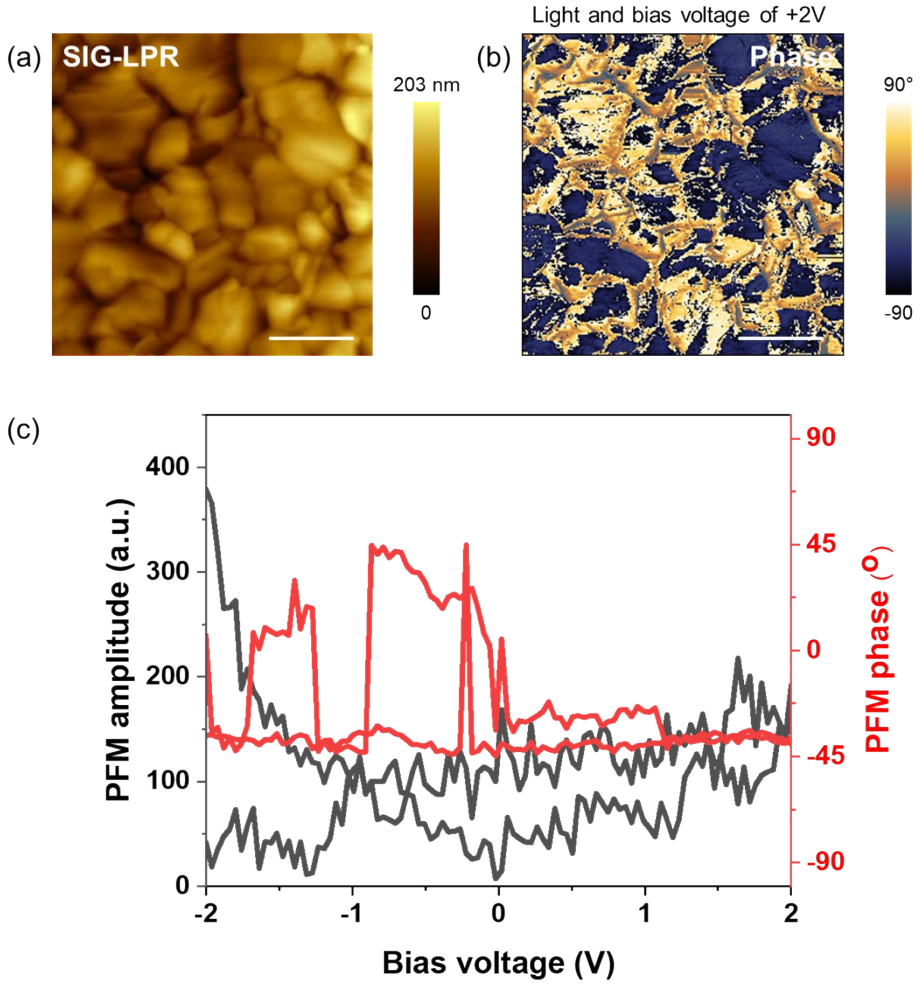

Supplementary Fig. 14. PFM measurements of SIG-LPR perovskite film. (a) Topography image, (b) Phase spatial map under illumination with a bias voltage of +2V, and (c) PFM amplitude- and phase-switching spectroscopy loops. The scale bars represent 1 μm.

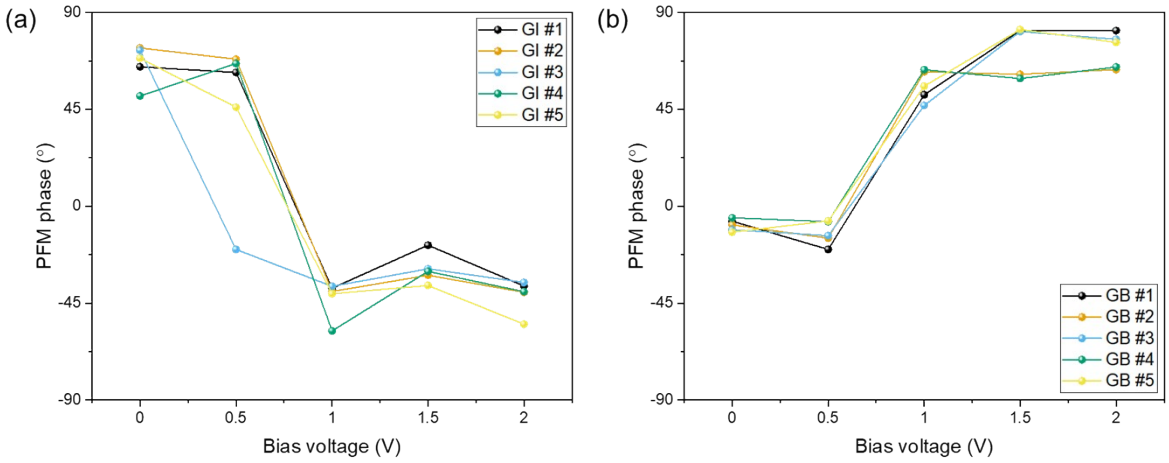

Supplementary Fig. 15. The evolution of phase responses as a function of bias voltage under illumination at (a) grain interiors (GIs), and (b) grain boundaries (GBs) of SIG-HPR perovskite film.

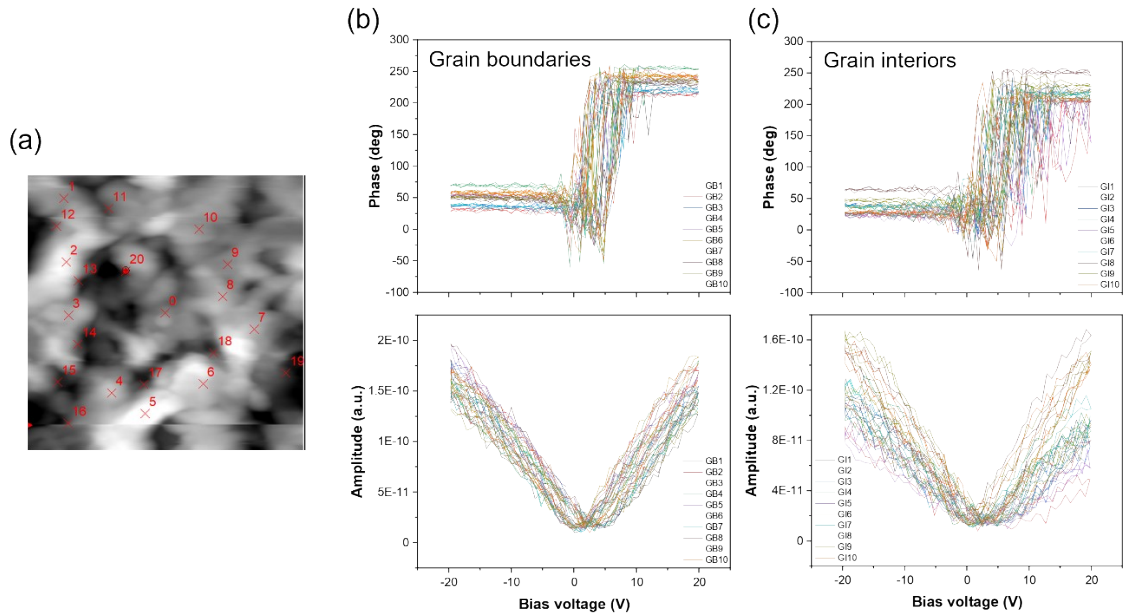

Supplementary Fig. 16. PFM spectroscopic measurements under illumination of SIG-HPR 2D (MA)PEA_2PbI_4 perovskite film. (a) Topography image, (b) PFM phase and amplitude loops at (b) GBs (points from 1-10), and (c) GIs (points from 11-20), respectively.

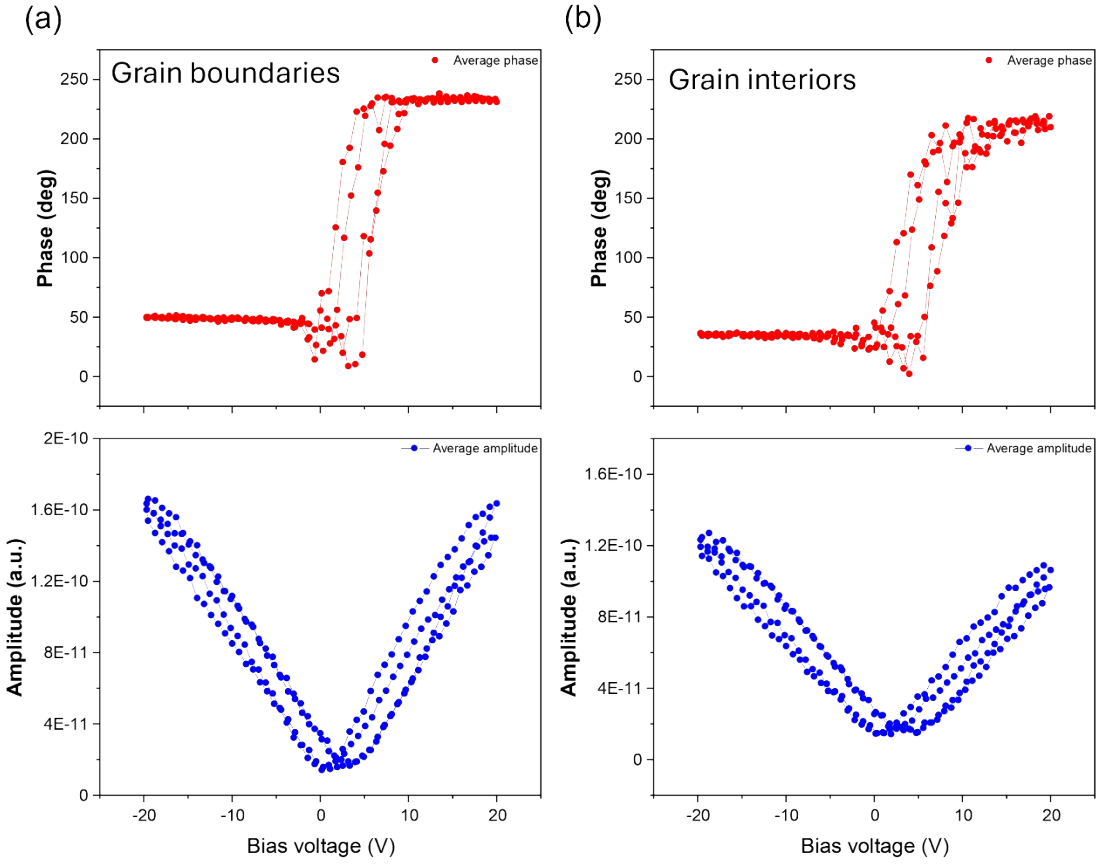

Supplementary Fig. 17. The averaged PFM phase and amplitude responses under illumination from **Supplementary Fig. 16** for (a) GBs and (b) GIs.

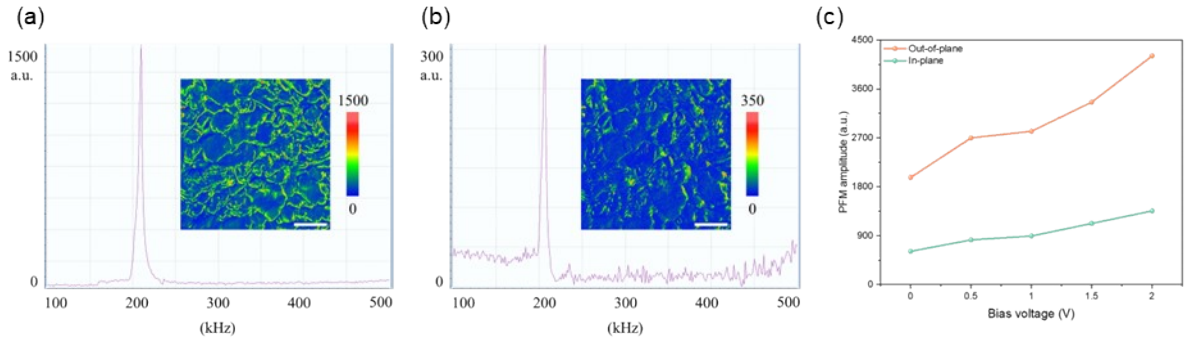

Supplementary Fig. 18. Contact resonance frequency for (a) out-of-plane PFM amplitude response where the inset represents out-of-plane PFM spatial map, (b) in-plane PFM amplitude response where the inset represents in-plane PFM spatial map, and (c) Out-of-plane and in-plane PFM responses of HPR film as a function of bias voltage.

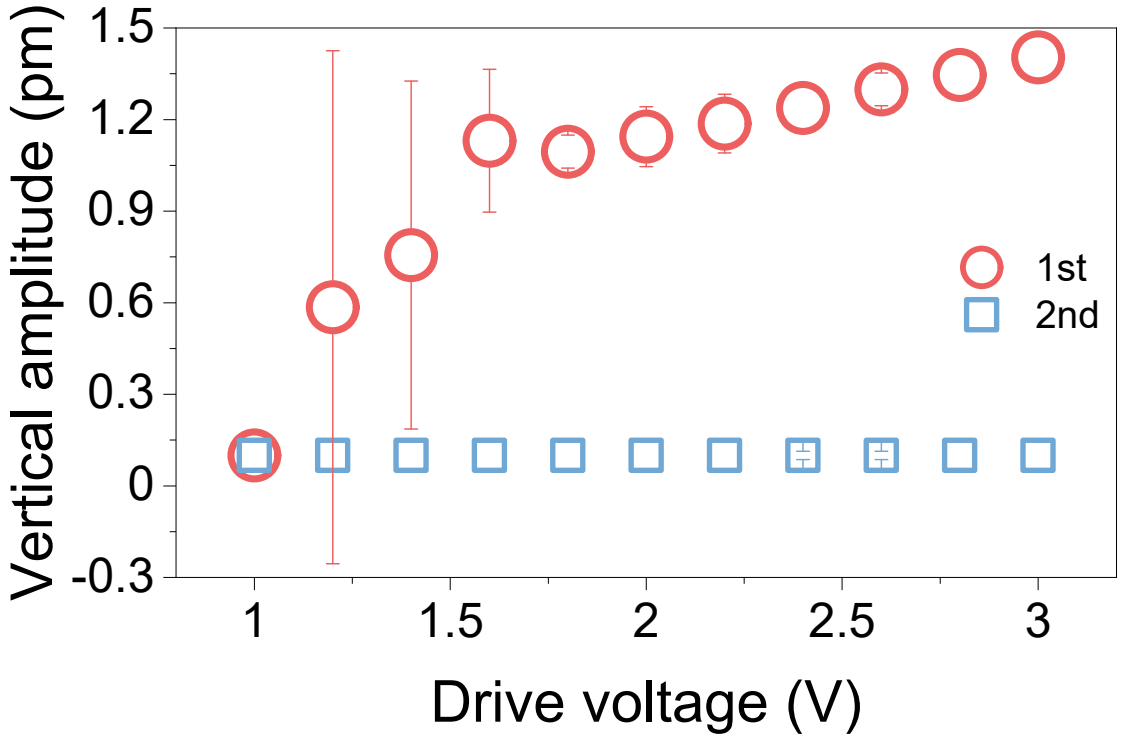

Supplementary Fig. 19. Vertical amplitude (1st and 2nd harmonic signals) versus AC drive voltage in PFM of SIG-HPR 2D (MA)PEA_2PbI_4 perovskite.

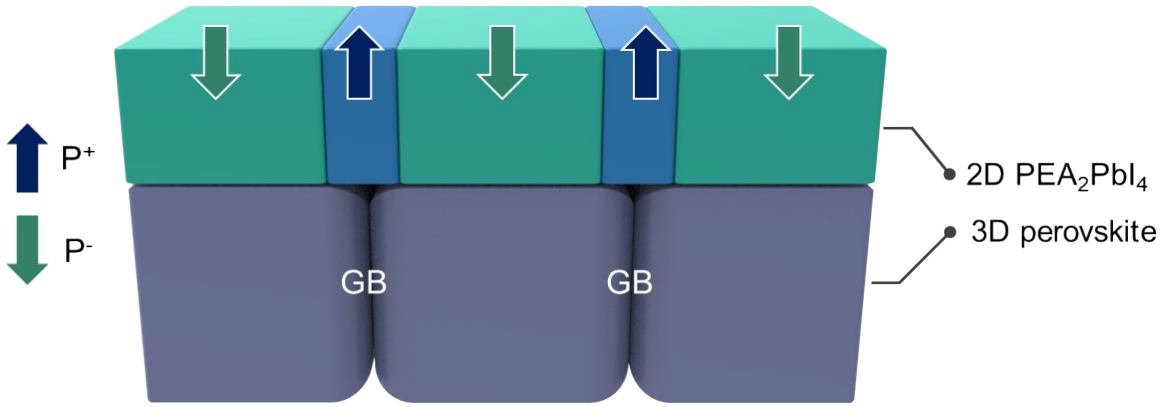

Supplementary Fig. 20. Schematic of net out-of-plane polarization in SIG-HPR perovskite film. A major polarization difference appears directly in the upper regions of the grain boundaries and grain interiors of 3D perovskite layer.

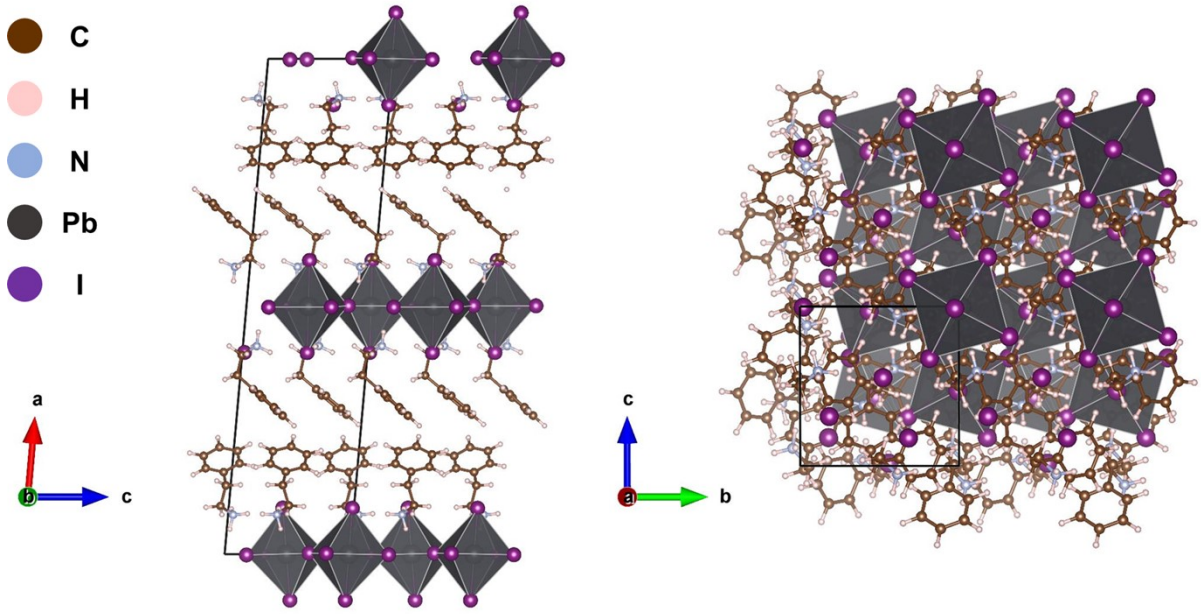

Supplementary Fig. 21. 2D/3D perovskite ferroelectric non-centrosymmetric structure.

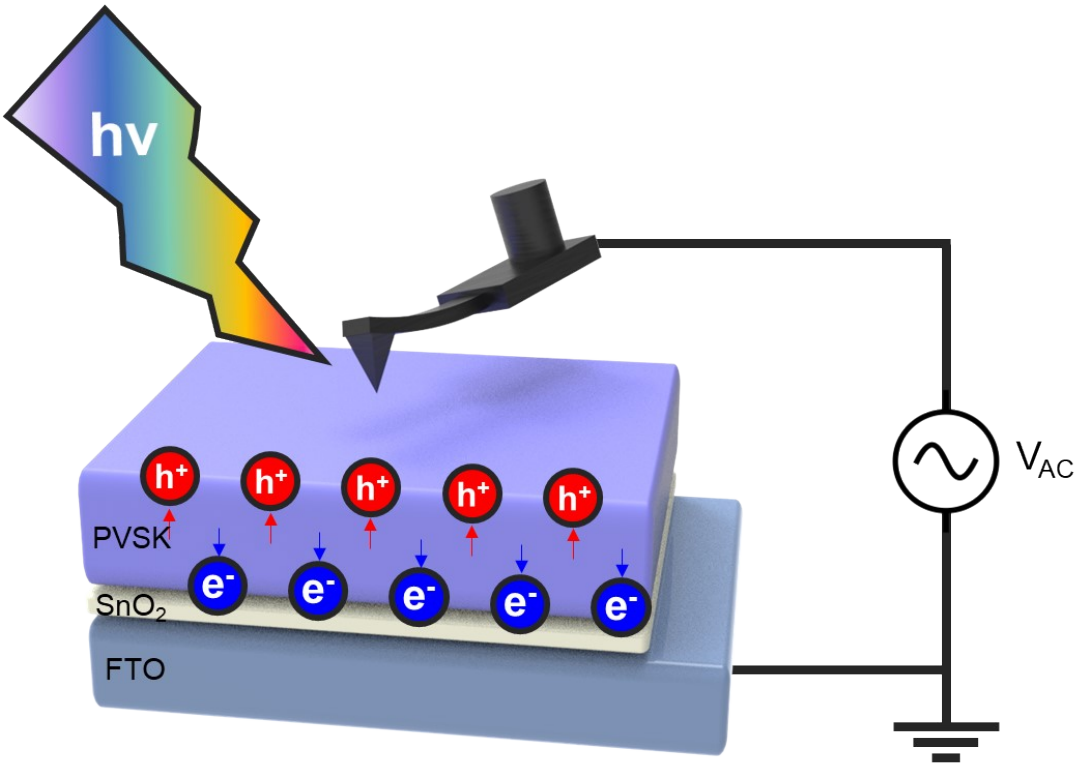

Supplementary Fig. 22. Schematic diagram of KPFM measurement representing charge transport in the perovskite film under illumination.

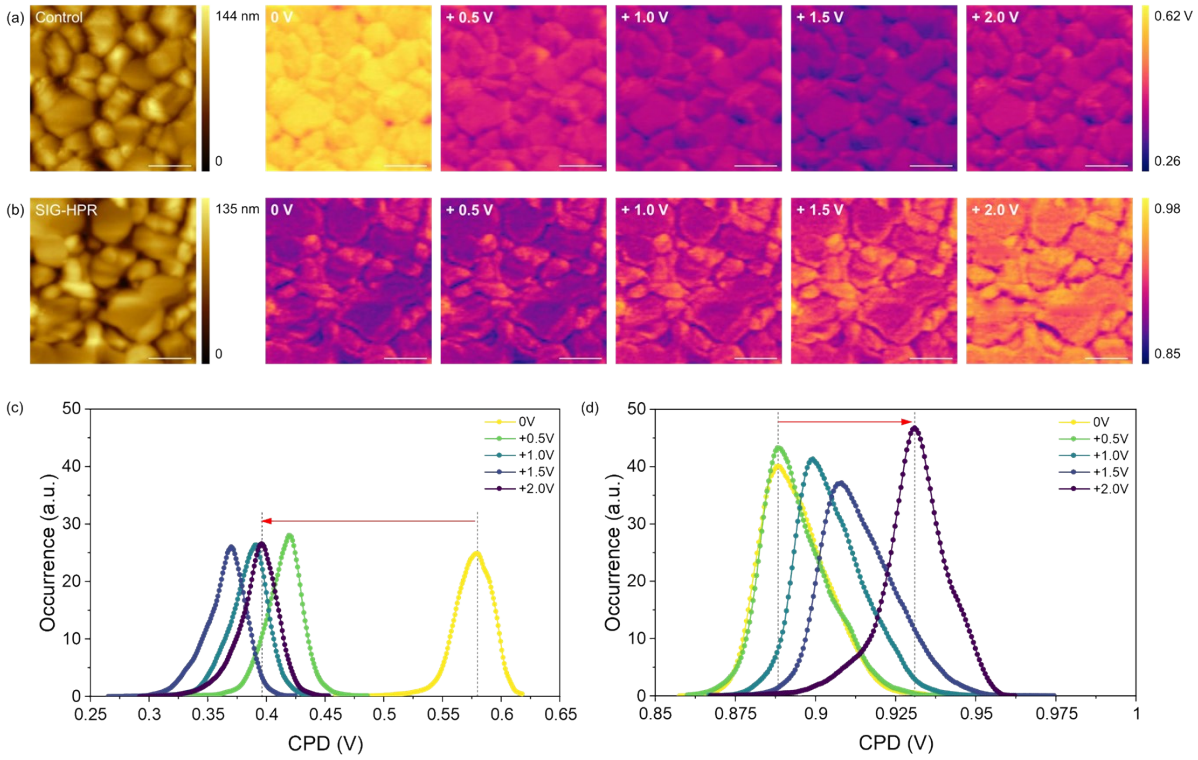

Supplementary Fig. 23. Light- and bias-dependent KPFM measurements of (a) control, and (b) SIG-HPR perovskite films under illumination with applied bias voltage from 0 to + 2 V with an increment

of 0.5 V, and corresponding CPD distribution curves for (c) control, and (d) SIG-HPR perovskite films. The scale bar represents 1 μm.

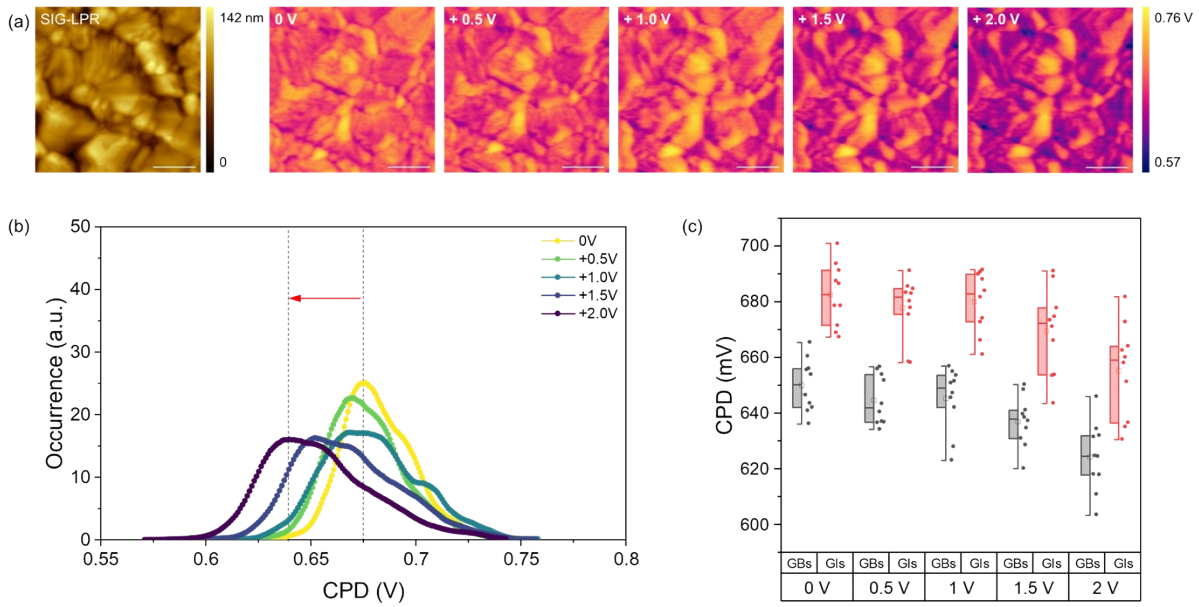

Supplementary Fig. 24. (a) Light- and bias-dependent KPFM measurements of SIG-LPR perovskite film under illumination with applied bias voltage from 0 to + 2 V with an increment of 0.5 V, and (b) corresponding CPD distribution curves and (c) statistics of CPD at GBs and GIs. The scale bar represents 1 μm.

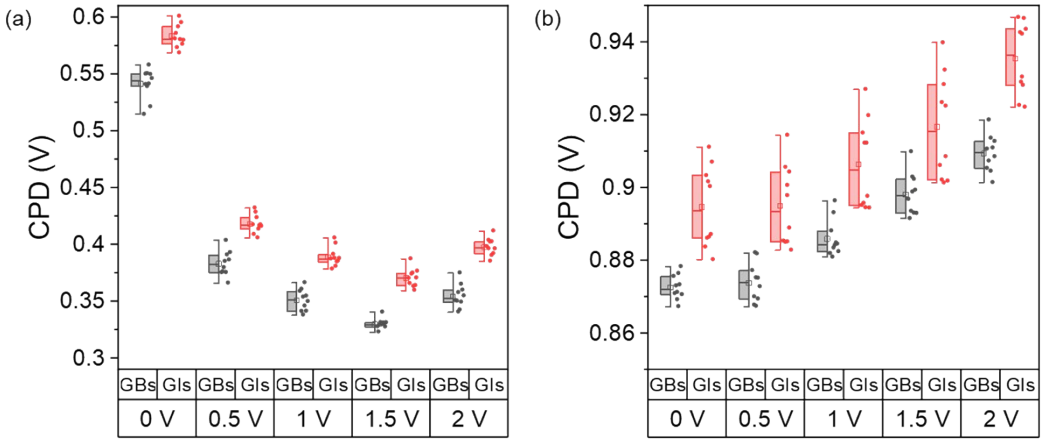

Supplementary Fig. 25. The statistics of CPD at GBs and GIs for (a) control, and (b) SIG-HPR perovskite films as a function of the different bias voltages under illumination.

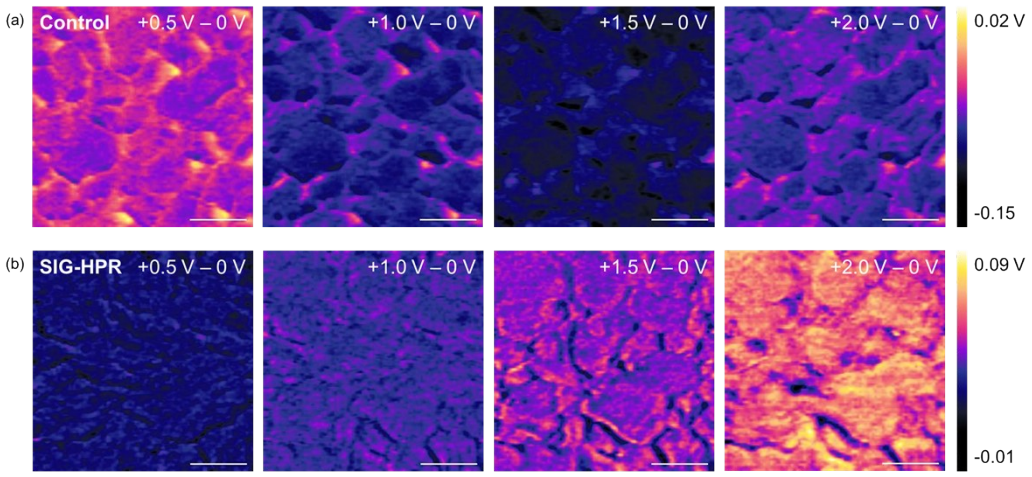

Supplementary Fig. 26. The subtracted CPD spatial maps at each bias voltage under illumination for (a) control, and (b) SIG-HPR perovskite films. The scale bar represents 1 μm.

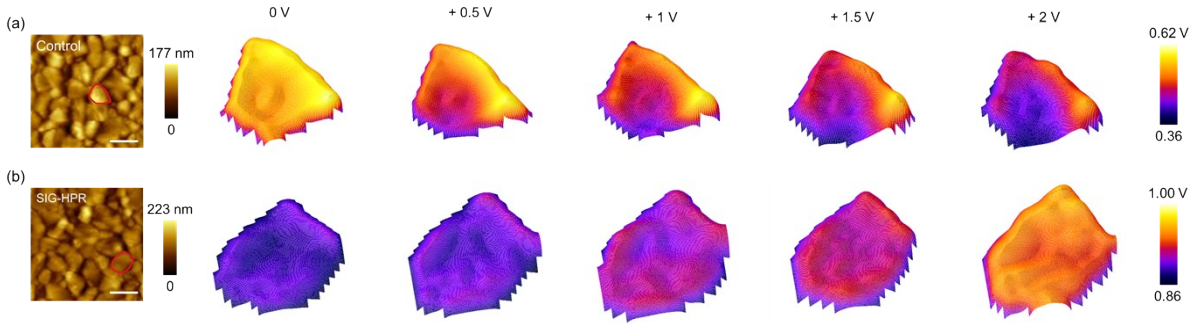

Supplementary Fig 27. 3D CPD distribution within the individual grains of (a) control, and (b) SIG-HPR perovskite films under illumination with applied voltages from 0 V to + 2 V. The scale bar represents 1 μm.

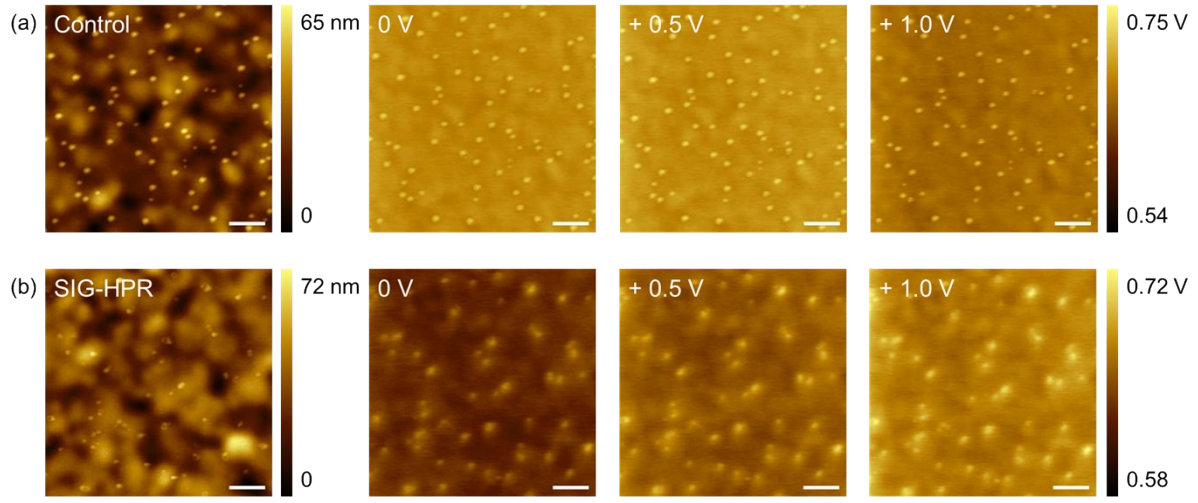

Supplementary Fig. 28. Light- and bias-dependent KPFM measurement of a HTL layer (Spiro-OMeTAD) on top of (a) control, and (b) SIG-HPR perovskite films. The scale bar represents 1 μm.

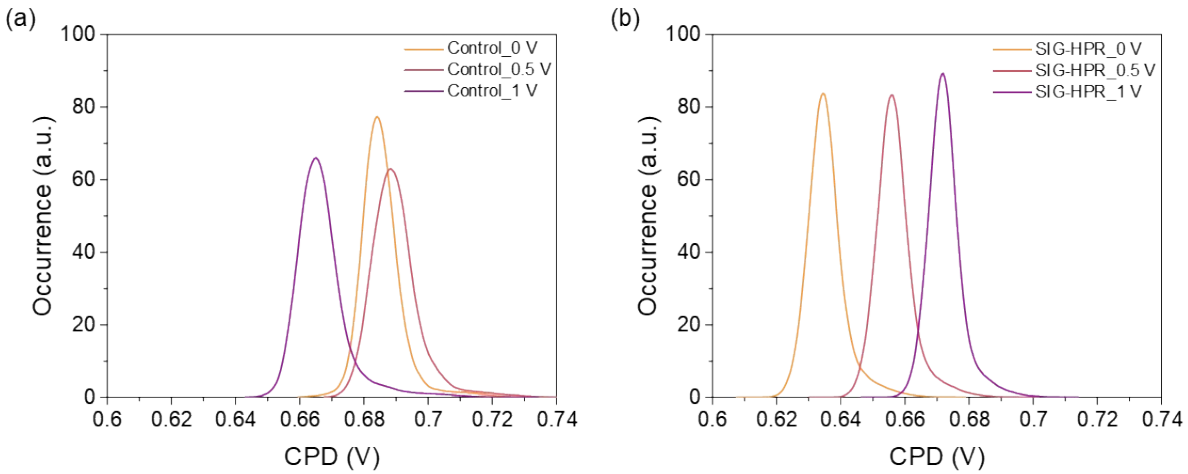

Supplementary Fig. 29. CPD distribution curves of a HTL layer (Spiro-OMeTAD) on top of (a) control, and (b) SIG-HPR perovskite films.

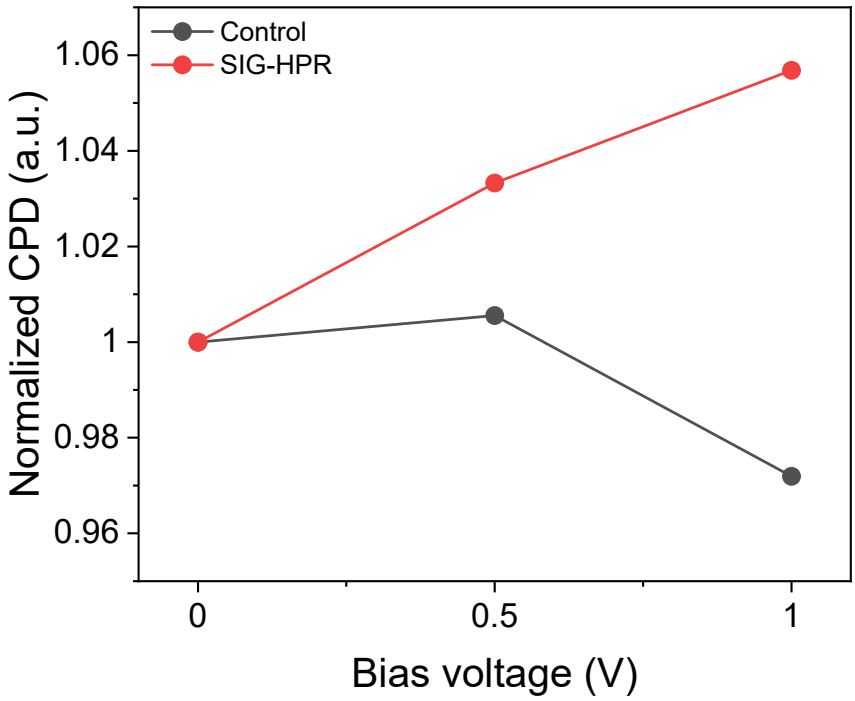

Supplementary Fig. 30. Normalized CPD plot of control, and SIG-HPR films, as a function of bias voltage from 0 V to + 1 V with an increment of + 0.5 V.

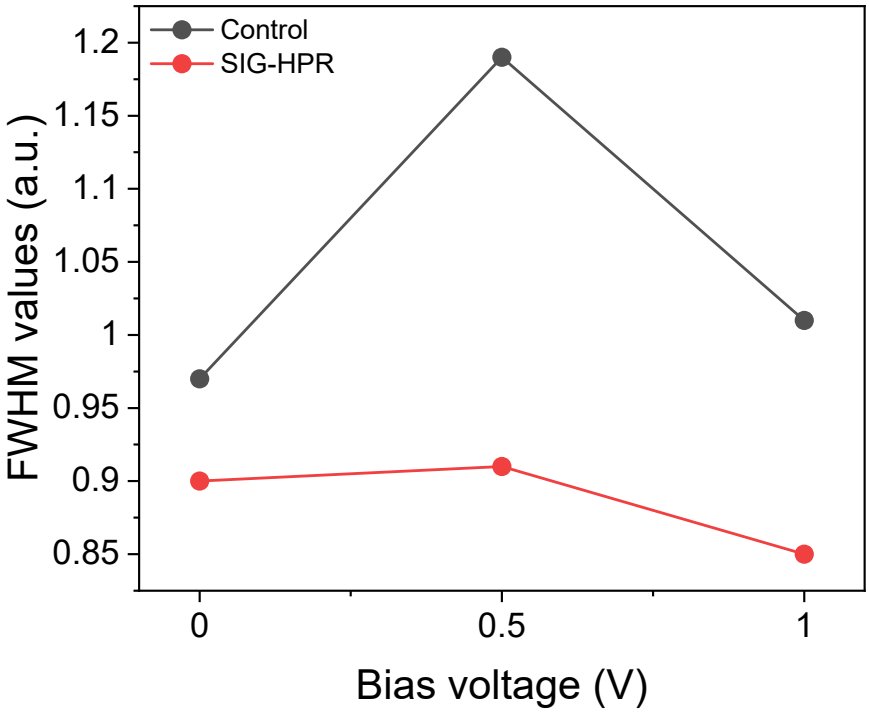

Supplementary Fig. 31. FWHM values of control and SIG-HPR films obtained from CPD distribution curves shown in **Supplementary Fig. 29**.

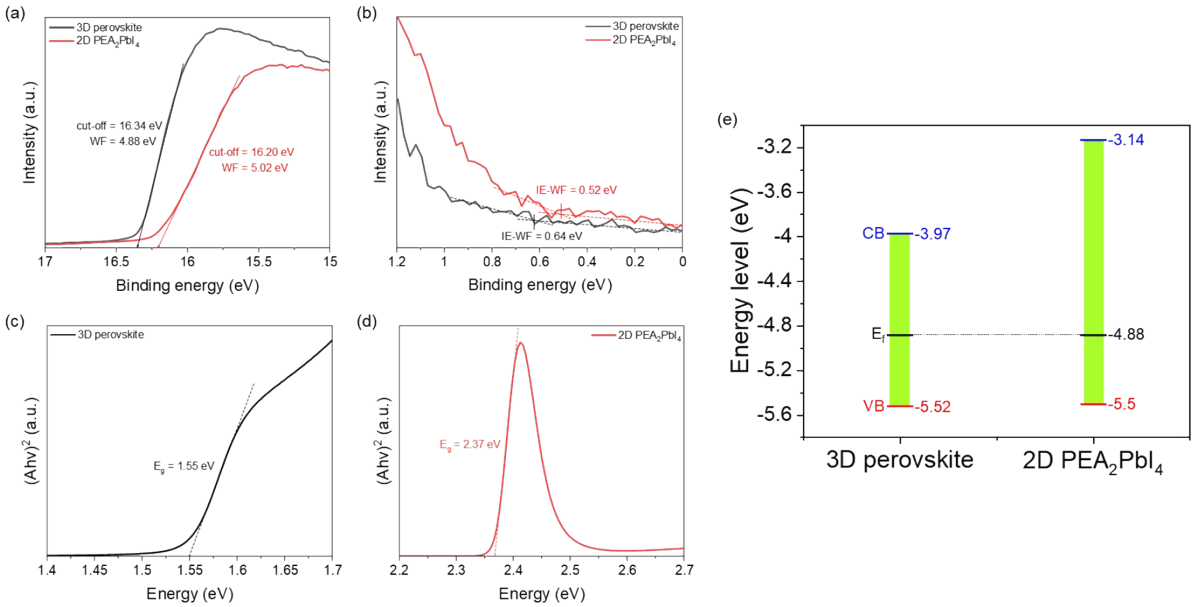

Supplementary Fig. 32. UPS measurement. (a) UPS spectra around the secondary electron cut-off, (b) UPS spectra in the valence band (VB) region, absorption curves of (c) 3D $(FAPbI_3)_{0.95}(MAPbBr_3)_{0.05}$ perovskite, and (d) 2D PEA_2PbI_4 perovskite, and (e) Fermi level aligned energy level diagram of 3D perovskite, and 2D PEA_2PbI_4 perovskite films.

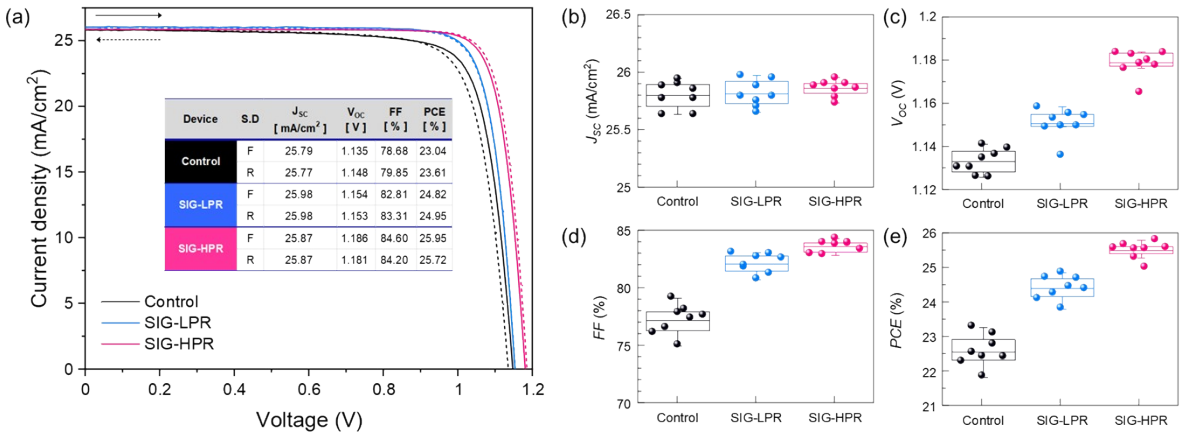

Device	S.D	J_{SC} [mA/cm^2]	V_{OC} [V]	FF [%]	PCE [%]
Control	F	25.79	1.135	78.68	23.04
	R	25.77	1.148	79.85	23.61
SIG-LPR	F	25.98	1.154	82.81	24.82
	R	25.98	1.153	83.31	24.95
SIG-HPR	F	25.87	1.186	84.60	25.95
	R	25.87	1.181	84.20	25.72

Supplementary Fig. 33. (a) J-V curves of the champion device along with (b-e) the statistical analysis of device performance for control, SIG-LPR, and SIG-HPR perovskite devices.

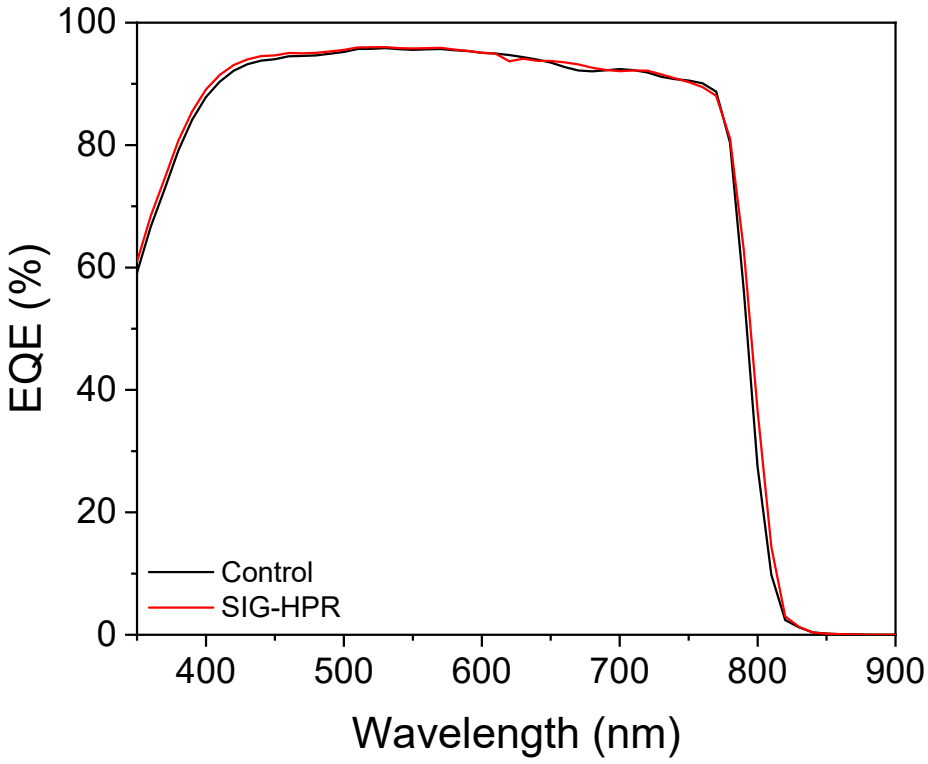

Supplementary Fig. 34. EQE spectra of the representative control and SIG-HPR devices.

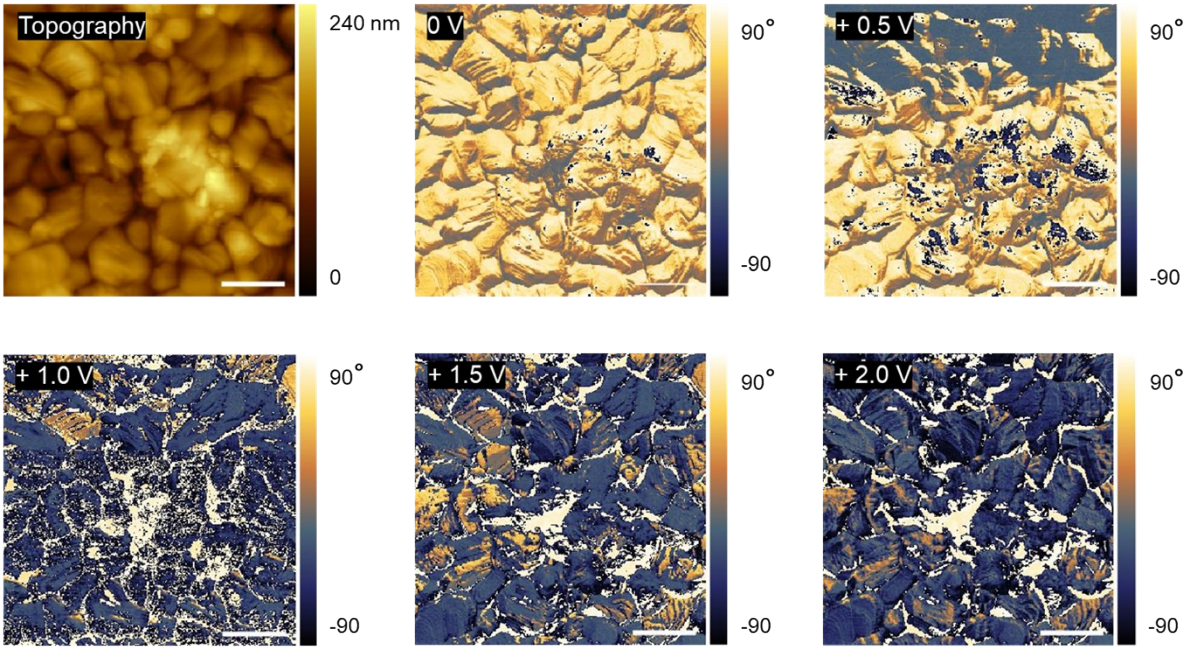

Supplementary Fig. 35. Light- and bias- dependent PFM phase measurements of SIG-HPR perovskite film, from bias voltages of 0 to + 2 V. The scale bar represents 1 μm.

4.2 One-Sun Current-Voltage (I-V) Characteristics Measurement

The I-V parameters of the test solar cell are shown below.

Table 4. Main I-V parameters for the test solar cell

Sample ID	Open-circuit voltage V_{oc} (V)	Short-circuit current I_{sc} (mA)	Fill factor FF (%)	Area A (cm^2)	Efficiency η (%)
A2 Averaged	1.177	2.51	82.82	0.097	25.18
Forward	1.176	2.51	82.52	-	25.08
Reverse	1.177	2.51	83.19	-	25.29

Table 5. Other I-V parameters for the test solar cell

Sample ID	Voltage at max. power V_{mpp} (V)	Current at max. power I_{mpp} (mA)	Maximum power P_{mpp} (mW)	Short-circuit current density J_{sc} (mA/cm^2)	Mismatch correction factor
A2 Averaged	1.022	2.39	2.44	25.84	1.0059
Forward	1.016	2.40	2.43	25.85	-
Reverse	1.024	2.40	2.45	25.82	-

The I-V parameters are computed from average of the forward and reverse I-V sweep measurements, performed at a sweep rate of 0.10 V/s. The relative difference of FF for forward and reverse I-V sweep at this sweep rate was less than 1%.
The I-V parameters reported are applicable to the time of the test, and do not imply future performance.

The plot of the test solar cell I-V characteristics is shown below.

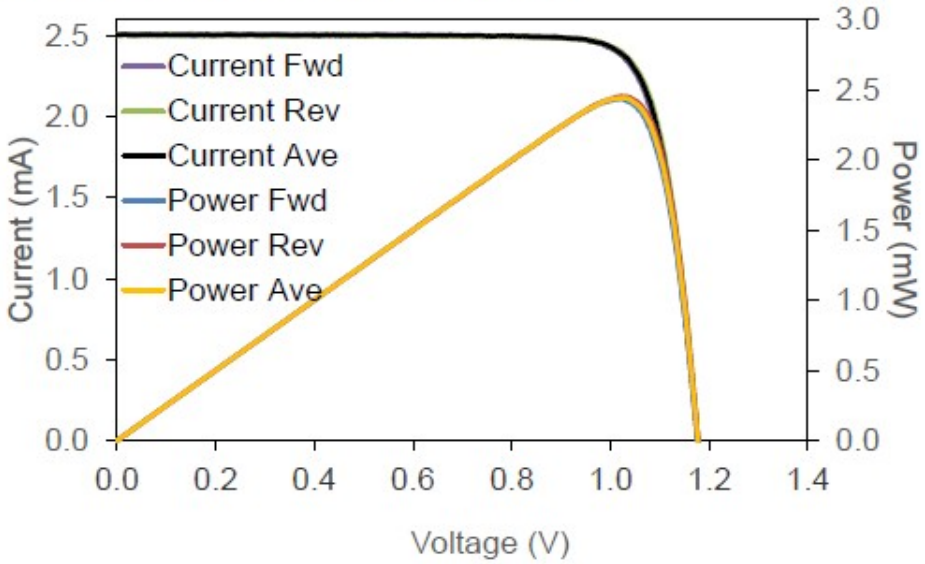

Figure 2. I-V characteristics of test solar cell

Supplementary Fig. 36. Independent certification from Solar Energy Research Institute of Singapore (SERIS), confirming a power conversion efficiency of 25.18 %.

Table S1. Comparison of the J-V parameters for the ferroelectric 2D/3D junction perovskite solar cell in this study with previously reported literature.

Year	3D perovskite	M*	2D perovskite	PCE	J_{SC}	V_{OC}	FF	Ref.
2021	$FA_{0.95}MA_{0.05}Pb(I_{0.95}Br_{0.05})_3$ with MACl	1.4	$(BA)_2PbI_4$	24.59	24.70	1.185	83.90	[5]
2022	$FA_{0.99}MA_{0.01}Pb(I_{0.99}Br_{0.01})_3$ with MACl	1.81	OAI	25.1	25.52	1.175	83.88	[6]
2023	$FAPbI_3$:3APX (X=I, Br, Cl) with MACl	1.5	PEAI	25.3	26.04	1.181	82.21	[7]
2023	$Cs_{0.05}MA_{0.05}FA_{0.9}PbI_3$	1.4	PEAI	25.0	26.2	1.15	82.0	[8]
2024	$FAPbI_3$ with MACl	1.4	PTABr	25.31	25.84	1.182	82.9	[9]
2024	$FAPbI_3$ with MACl	2.3	OAI	25.63	26	1.191	82.77	[10]
2024	$FAPbI_3$ with MACl	1.6	PEAI	26.14	25.97	1.18	85.04	[11]
2024	$FAPbI_3$ with MACl	1.8	$(BA)_2PbBr_4$	25.37	26.08	1.174	82.76	[12]
2024	$FAPbI_3$ with MACl	1.8	BAE	26.52	26.28	1.175	85.9	[13]
2024	$FA_{0.992}MA_{0.008}Pb(I_{0.992}Br_{0.008})_3$ with MACl	1.52	HABr	25.3	25.2	1.18	84.9	[14]
2025	$FAPbI_3$ with MACl	1.9	OAI	26.18	26.18	1.19	84.2	[15]
2025	$Cs_{0.03}(FA_{0.97}MA_{0.03})_{0.97}Pb(I_{0.97}Br_{0.03})_3$ with MACl	1.5	BABr	25.22	25.51	1.22	81.03	[16]
2025	$FAPbI_3$ with MACl	1.8	OAI	25.7	26.1	1.16	84.8	[17]
2025	**$FAPbI_3$ with MACl**	**1.67**	**SIG-HPR $(PEA)_2PbI_4$**	**25.18**	**25.88**	**1.177**	**82.82**	**This work**

References

1 H.-H. Fang, J. Yang, S. Tao, S. Adjokatse, M. E. Kamminga, J. Ye, G. R. Blake, J. Even and M. A. Loi, *Adv Funct Mater*, 2018, **28**, 1800305.

2 Q. Zhang, A. Solanki, K. Parida, D. Giovanni, M. Li, T. L. C. Jansen, M. S. Pshenichnikov and T. C. Sum, *ACS Appl Mater Interfaces*, 2019, **11**, 13523–13532.

3 Y. Zhai, S. Baniya, C. Zhang, J. Li, P. Haney, C.-X. Sheng, E. Ehrenfreund and Z. V. Vardeny, *Sci Adv*, 2023, **3**, e1700704.

4 J. J. Yoo, G. Seo, M. R. Chua, T. G. Park, Y. Lu, F. Rotermund, Y.-K. Kim, C. S. Moon, N. J. Jeon, J.-P. Correa-Baena, V. Bulović, S. S. Shin, M. G. Bawendi and J. Seo, *Nature*, 2021, **590**, 587–593.

5 Y.-W. Jang, S. Lee, K. M. Yeom, K. Jeong, K. Choi, M. Choi and J. H. Noh, *Nat Energy*, 2021, **6**, 63–71.

6 T. Zhang, F. Wang, H.-B. Kim, I.-W. Choi, C. Wang, E. Cho, R. Konefal, Y. Puttisong, K. Terado, L. Kobera, M. Chen, M. Yang, S. Bai, B. Yang, J. Suo, S.-C. Yang, X. Liu, F. Fu, H. Yoshida, W. M. Chen, J. Brus, V. Coropceanu, A. Hagfeldt, J.-L. Brédas, M. Fahlman, D. S. Kim, Z. Hu and F. Gao, *Science (1979)*, 2022, **377**, 495–501.

7 T. Yang, L. Gao, J. Lu, C. Ma, Y. Du, P. Wang, Z. Ding, S. Wang, P. Xu, D. Liu, H. Li, X. Chang, J. Fang, W. Tian, Y. Yang, S. (Frank) Liu and K. Zhao, *Nat Commun*, 2023, **14**, 839.

8 P. Shi, Y. Ding, B. Ding, Q. Xing, T. Kodalle, C. M. Sutter-Fella, I. Yavuz, C. Yao, W. Fan, J. Xu, Y. Tian, D. Gu, K. Zhao, S. Tan, X. Zhang, L. Yao, P. J. Dyson, J. L. Slack, D. Yang, J. Xue, M. K. Nazeeruddin, Y. Yang and R. Wang, *Nature*, 2023, **620**, 323–327.

9 C. Huang, S. Tan, B. Yu, Y. Li, J. Shi, H. Wu, Y. Luo, D. Li and Q. Meng, *Joule*, 2024, **8**, 2539–2553.

10 H. Song, H.-B. Kim, S. C. Cho, J. Lee, J. Yang, W. H. Jeong, J. Y. Won, H. I. Jeong, J. Yeop, J. Y. Kim, B. J. Lawrie, M. Ahmadi, B. R. Lee, M. Kim, S. J. Choi, D. S. Kim, M. Lee, S. U. Lee, Y. Jo and H. Choi, *Joule*, 2024, **8**, 2283–2303.

11 M. J. Paik, Y. Y. Kim, J. Kim, J. Park and S. Il Seok, *Joule*, 2024, **8**, 2073–2086.

12 S. Lee, H. Cho, S. Kang, O. J. Oh, D. H. Kim and J. H. Noh, *Energy Environ Sci*, 2024, **17**, 6234–6244.

13 Q. Li, H. Liu, C.-H. Hou, H. Yan, S. Li, P. Chen, H. Xu, W.-Y. Yu, Y. Zhao, Y. Sui, Q. Zhong, Y. Ji, J.-J. Shyue, S. Jia, B. Yang, P. Tang, Q. Gong, L. Zhao and R. Zhu, *Nat Energy*, 2024, **9**, 1506–1516.

14 D. W. deQuilettes, J. J. Yoo, R. Brenes, F. U. Kosasih, M. Laitz, B. D. Dou, D. J. Graham, K. Ho, Y. Shi, S. S. Shin, C. Ducati, M. G. Bawendi and V. Bulović, *Nat Energy*, 2024, **9**, 457–466.

15 Y. S. Shin, J. W. Song, D. G. Lee, J. Lee, J. Seo, J. Roe, G. Y. Shin, D. Kim, J. Yeop, D. Lee, M. Kim, Y. Jo, H. Jang, J. G. Son, W. Lee, J. Son, S. Park, S. Cho, T. J. Shin, G.-H. Kim, J. Y. Kim, T. K. Lee, M. Grätzel and D. S. Kim, *Joule*, 2025, **9**, 101779.

16 Q. Liang, K. Liu, Y. Han, H. Xia, Z. Ren, D. Li, T. Zhu, L. Cheng, Z. Wang, C. Zhu, P. W. K. Fong, J. Huang, Q. Chen, Y. Yang and G. Li, *Nat Commun*, 2025, **16**, 190.

17 D. Koo, Y. Choi, U. Kim, J. Kim, J. Seo, E. Son, H. Min, J. Kang and H. Park, *Nat Nanotechnol*, 2025, **20**, 75–82.